$D(\phi) = \Delta V^2 \tau_d$. We approximate the behaviour of the decay time with $\tau_d = \xi/2.5\Delta V$, and use the measured functional form for ξ, and the expression for ΔV in equation (2), thereby obtaining a new analytic expression for the diffusion coefficient, $D(\phi) = 11.4aV_0\{\eta_0/[\eta(\phi)]\}[S(\phi,0)]^{1/2}$. We again obtain very good agreement with the data, as shown by the solid line in Fig. 4. This agreement further validates our use of thermal equilibrium quantities to describe this highly athermal system.

We can obtain insight into the origin of the thermalization of the sedimenting particles by considering the diffusion coefficient. We take the approximate relation based on our data, $D(\phi) \approx \Delta V\xi/2.5$, and use equation (1) for the velocity fluctuations, to obtain

$$D(\phi) = \frac{C_1 \Delta m_\xi g \xi}{6\pi\eta(\phi)\xi} \quad (3)$$

where $C_1 \approx 0.4$. This expression has the same functional form as the Stokes–Einstein equation for the diffusion coefficient of thermalized particles. This allows us to identify the effective temperature, $k_B T = C_1 \Delta m_\xi g \xi$, which provides the equivalent of thermal energy to the system allowing it to explore phase space, and resulting in the diffusive motion of the particles. But, here it is clearly the gravitational energy of the fluctuation in particle density which drives the thermalization. We note that it is only the fluctuating part of the energy, that arising from Δm_ξ, which drives the system and causes the diffusive motion. By contrast, the full buoyant mass of the particles is much larger, but contributes only to the average settling, and not to the fluctuations which are the origin of the thermalization. The conversion of potential energy into viscous shear energy, rather than translational kinetic energy, is a consequence of the vanishingly small Reynolds number; Re is related to the ratio of kinetic to shear energy.

Finally, we note that the effective temperature can only be defined for the parallel component of the motion; in the perpendicular direction, there is no gravitational potential energy. The difference in the parallel and perpendicular components of the diffusion coefficients suggest that the effective temperature also exhibits an asymmetry[12]; for the perpendicular temperature it must be the coupling of the two components of the velocity fluctuations that causes the thermalization and leads to the diffusive motion. Nevertheless, these results provide a clear measure of the effective temperature for sedimenting particles, and offer new insight into the relationship between the diffusive motion of individual particles and collective correlations of the velocity fluctuations. □

Received 6 October; accepted 30 November 2000.

1. Segrè, P. N., Herbolzheimer, E. & Chaikin, P. M. Long-range correlations in sedimentation. *Phys. Rev. Lett.* **79,** 2574–2577 (1997).
2. Xue, J.-Z., Herbolzheimer, E., Rutgers, M. A., Russel, W. B. & Chaikin, P. M. Diffusion, dispersion, and settling of hard spheres. *Phys. Rev. Lett.* **69,** 1715–1718 (1992).
3. Tong, T. & Ackerson, B. J. Analogies between colloidal sedimentation and turbulent convection at high Prandtl numbers. *Phys. Rev. E* **58,** R6931–R6934 (1998).
4. Levine, A., Ramaswamy, S., Frey, E. & Bruinsma, R. Screened and unscreened phases in sedimenting suspensions. *Phys. Rev. Lett.* **81,** 5944–5947 (1998).
5. Caflisch, R. E. & Luke, J. H. C. Variance in the sedimentation speed of a suspension. *Phys. Fluids* **28,** 759–760 (1985).
6. Hinch, E. J. in *Disorder and Mixing* (eds Guyon, E., Nadal, J.-P. *et al.* Pomeau, Y.) 153–185 (Kluwer Academic, Dordrecht, 1988).
7. Koch, D. L. & Shaqfeh, E. S. G. Screening in sedimenting suspensions. *J. Fluid Mech.* **224,** 276–303 (1991).
8. Brenner, M. P. Screening mechanisms in sedimentation. *Phys. Fluids* **11,** 754–772 (1999).
9. Adrian, R. J. Particle-imaging techniques for experimental fluid mechanics. *Annu. Rev. Fluid Mech.* **23,** 261–304 (1991).
10. Cowan, M. L., Page, J. H. & Weitz, D. A. Velocity correlations in fluidized suspensions probed by ultrasonic correlation spectroscopy. *Phys. Rev. Lett.* **85,** 453–456 (2000).
11. Nicolai, H. & Guazelli, E. Effect of the vessel size on the hydrodynamic diffusion of sedimenting spheres. *Phys. Fluids* **7,** 3–5 (1995).
12. Nicolai, H., Herzhaft, B., Hinch, E. J., Oger, L. & Guazelli, E. Particle velocity fluctuations and hydrodynamic self-diffusion of sedimenting non-Brownian spheres. *Phys. Fluids* **7,** 12–23 (1995).
13. Russel, W. B., Saville, D. A. & Schowalter, W. R. *Colloidal Dispersions* (Cambridge Univ. Press, Cambridge, 1989).
14. Richardson, J. F. & Zaki, W. N. Sedimentation and fluidization I. *Trans. Inst. Chem. Eng.* **32,** 35–53 (1954).
15. de Kruif, C. G., van Iersel, E. M. F., Vrij, A. & Russel, W. B. Hard sphere colloidal dispersions: viscosity as a function of shear rate and volume fraction. *J. Phys. Chem.* **83,** 4717–4725 (1985).
16. Bender, J. W. & Wagner, N. J. Reversible shear thickening in monodisperse and bidisperse colloidal dispersions. *J. Rheol.* **40,** 899–916 (1996).

Acknowledgements

We thank M. Brenner, S. Tee, P. Tong, A. J. C. Ladd, B. J. Ackerson, P. Mucha and A. Levine for discussions. This work was supported by NASA, NSF and the donors of the Petroleum Research Fund, administered by the ACS. Current address of P.N.S. is NASA MSFC, Huntsville, AL 35802 (Phil.Segre@msfc.nasa.gov).

Correspondence and requests for materials should be addressed to D.A.W. (e-mail: weitz@deas.harvard.edu) or P.N.S.

Pumping of nutrients to ocean surface waters by the action of propagating planetary waves

B. Mete Uz, James A. Yoder & Vladimir Osychny

Graduate School of Oceanography, University of Rhode Island, S. Ferry Road, Narragansett, Rhode Island 02882, USA

Primary productivity in the oceans is limited by the lack of nutrients in surface waters. These nutrients are mostly supplied from nutrient-rich subsurface waters through upwelling and vertical mixing[1], but in the ocean gyres these mechanisms do not fully account for the observed productivity[2]. Recently, the upward pumping of nutrients, through the action of eddies, has been shown to account for the remainder of the primary productivity; however, these were regional studies which focused on mesoscale (100-km-scale) eddies[3–6]. Here we analyse remotely sensed chlorophyll and sea-surface-height data collected over two years and show that 1,000-km-scale planetary waves, which propagate in a westward direction in the oceans, are associated with about 5 to 20% of the observed variability in chlorophyll concentration (after low-frequency and large-scale variations are removed from the data). Enhanced primary production is the likely explanation for this observation, and if that is the case, propagating disturbances introduce nutrients to surface waters on a global scale—similar to the nutrient pumping that occurs within distinct eddies.

Much of the motion in the open ocean is baroclinic: at the surface, geostrophic flow balances the pressure gradient caused by a sloping sea surface. The geostrophic current is typically strongest near the surface, and decreases with depth. Because the horizontal pressure gradient must similarly decrease with depth in order to maintain geostrophic balance, constant-density surfaces must slope in the opposite direction to the sea surface. As a result, a baroclinic disturbance that displaces the constant-density surfaces upwards has a negative sea surface height (SSH) anomaly, which can be measured by altimeters. These disturbances propagate westward—as planetary waves or eddies—mostly due to the variation of the Coriolis parameter with latitude. Westward-propagating first-mode baroclinic features dominate the propagating components of the SSH satellite-sensed record from the TOPEX/POSEIDON mission[7–9]. They have also been observed in images of sea surface temperature from the satellite-borne Advanced Very High Resolution Radiometer[10–12].

If the displacement of constant-density surfaces by baroclinic disturbances brought new nutrients into the euphotic zone, the concentration of phytoplankton chlorophyll would be expected to

increase above the disturbance. As the disturbance propagates westward, there would be enhanced production near the leading edge and fall-out and grazing of the biomass anomaly near the trailing edge, so that the chlorophyll anomaly would also propagate with the disturbance. If this were to happen, chlorophyll variability would have a component that was coherent with the SSH variations.

To look for this signature in the satellite imagery, we sought large-scale anomalies in SeaWiFS[13] remotely sensed oceanic chlorophyll concentration that propagate westward in coherence with SSH anomalies. Even though the eddy pumping mechanism was originally intended for mesoscale eddies, our study focuses on the larger scales of Rossby waves; this larger scale enables us to do more spatial smoothing and compositing (replacing cloud-masked pixels of one image with corresponding pixels of a consecutive image) over time. The compression of the upper layers of the ocean by a Rossby wave is very similar dynamically to the compression caused by a small-amplitude eddy, and the same mechanism of nutrient enhancement should apply. With a nonlinear eddy that transports water, the pumping would occur only once—during the spin-up of the eddy.

Propagating anomalies were readily observed as slanted features in time–longitude diagrams (Fig. 1) once data were bandpass-filtered to remove noise and variability at small scales as well as seasonal and other very-large-scale variations. These anomalies persisted for a long time. For example, a high-chlorophyll-concentration anomaly at 30° N which was at longitude −200° (160° E) around day 150 (150 days after 7 September 1997) was still visible on day 550, by which time it had moved to longitude −225° (135° E).

We used spectral analysis to investigate the coherence between chlorophyll and SSH features in order to separate different scales of variability and propagation directions. We calculated the power spectral density of—and coherence between—chlorophyll and SSH for individual ocean basins. At most latitudes, westward-propagating features made up almost all of the spectral density of SSH, whereas chlorophyll spectral density showed more spread. Part of the spread in the chlorophyll spectral density may be due to non-propagating phenomena such as the expansion of blooms in both directions. High coherence between chlorophyll and SSH was mostly in the westward-propagation quadrants (Fig. 2).

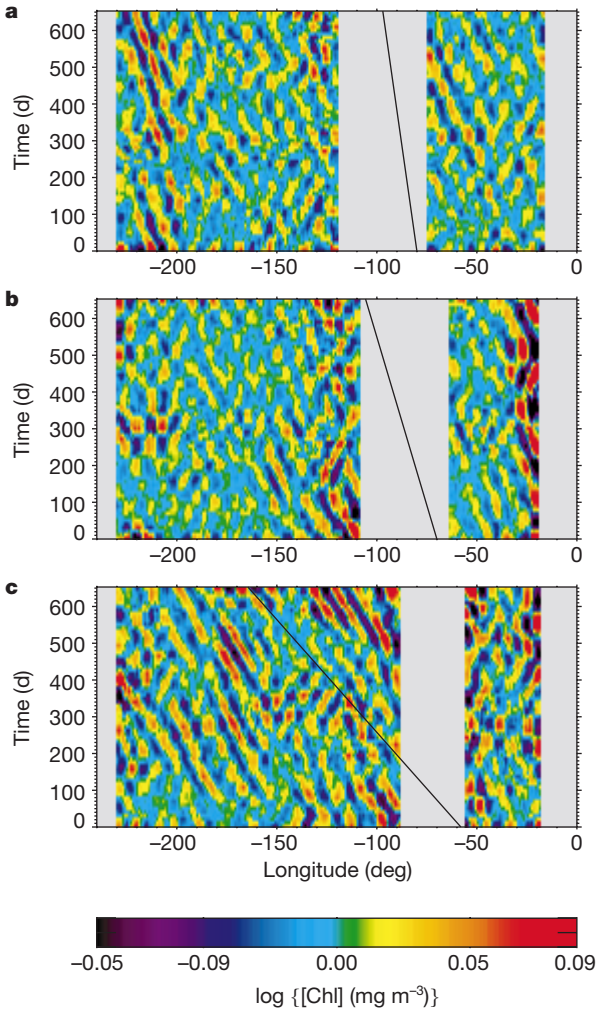

Figure 1 Time–longitude diagrams of the bandpass-filtered SeaWiFS chlorophyll concentration data. The figure shows zonal propagation of anomalies as slanted features. The phase speeds of linear non-dispersive first-mode baroclinic Rossby waves are shown by a solid line at each latitude (**a**, 30° N; **b**, 20° N; **c**, 10° N). The variation with latitude of the propagation speed of chlorophyll anomalies may be seen as an animation sequence at http://po.gso.uri.edu/~uz/chl_anomaly.htm).

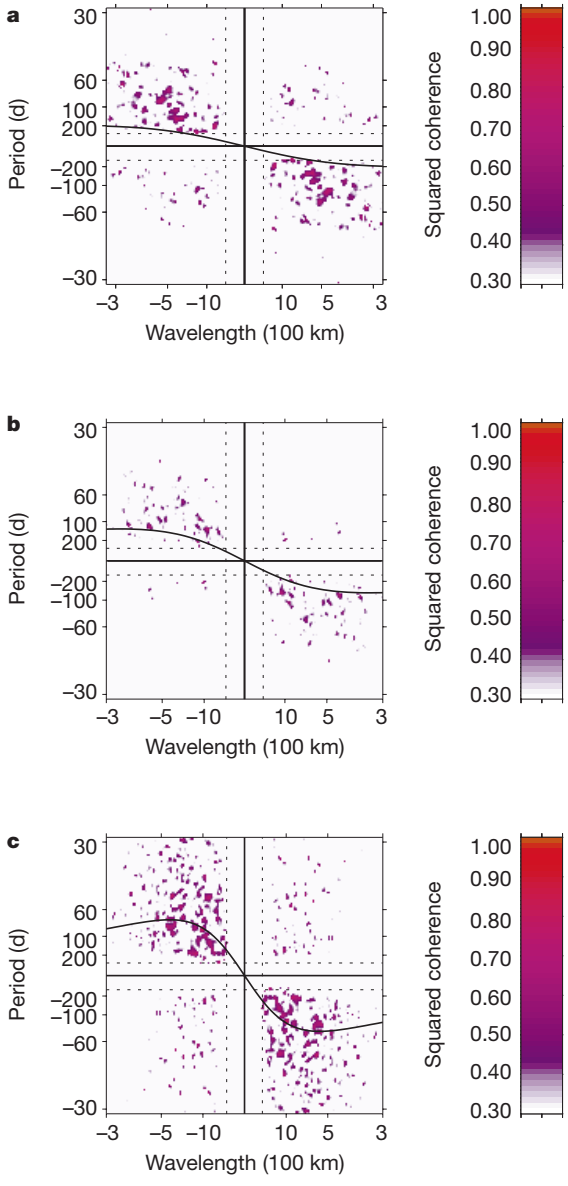

Figure 2 Wavenumber–frequency spectra of coherence between log(chlorophyll concentration) and sea surface height. Most of the spectral density is in the second and fourth quadrants, where propagation is westward. Data shown are from the Pacific Ocean at latitudes of 30° N (**a**), 20° N (**b**) and 10° N (**c**). Dotted lines bracketing the axes show cut-off points for the highpass filters. The linear dispersion relation is shown by a solid line.

Phase speeds of planetary waves measured with the TOPEX/POSEIDON altimeter have been seen to vary between 0.5 and 3 times the phase speed from the linear dispersion[7], though a recent study reports that with different methods the linear phase speed is within the error bars[14]. Nevertheless, the theoretical phase speed of baroclinic planetary waves may not be adequate for a precise comparison with measurements. Qualitatively, the propagation speeds of chlorophyll anomalies that we saw in the time–longitude diagrams were similar to the theoretical propagation speed of first-mode baroclinic planetary waves, and (more importantly) they varied with latitude in the same way.

We calculated propagation speeds from the chlorophyll and chlorophyll–SSH coherence spectra, and compared these to the non-dispersive linear phase speed calculated using climatological density profiles[15] (Fig. 3). Between 10° and 25° in both hemispheres, estimates from chlorophyll, SSH and chlorophyll–SSH coherence were all similar and within a factor of two of the theoretical phase speed. At higher latitudes (>25°), propagation speeds from chlorophyll spectra were significantly higher than the rest. This deviation must be caused by phenomena not related to SSH, because the propagation speed of the SSH coherent features (the estimate from chlorophyll–SSH coherence) remained close to the phase speed from SSH and the theoretical phase speed.

The confinement of high chlorophyll–SSH coherence in a localized area of the wavenumber–frequency domain allowed us to construct a filter to isolate chlorophyll features which were associated with the SSH anomalies. The variance of the coherent, westward-propagating signal was around 5–20% of the variance of the input (Fig. 4). These fractions depend on the choice of the threshold coherence, and are provided here as only a rough scale for the magnitude of the effect. This fraction varied with latitude, and between basins at any given latitude. There were local minima at latitudes corresponding to the middle of the subtropical gyres. The coherence estimate is sensitive to the relative magnitude of error in the data. If each data series is modelled as the sum of an ideal signal and random noise, wherever the amplitudes of the signals are reduced, the coherence estimate also goes down even though the coherence between the two ideal signals remains the same. This effect may be what we are seeing in the middle of the gyres, where the mean as well as the variability of chlorophyll is low and therefore the noise figure is high. The local minima at these locations may then be mostly in the estimate, and might not occur in the estimates if more accurate data were available. Nevertheless, in all basins there were large areas where coherence was observed between chlorophyll and SSH. We note that our analysis used the entire time record; for chlorophyll and SSH features to be coherent, they must not only coincide in space at one point in time, but they must propagate together. A phase offset may exist between chlorophyll and SSH features without reducing the coherence as long as the offset remains constant.

The mechanism of enhanced primary production proposed in ref. 3 may explain how the chlorophyll anomaly can follow the baroclinic disturbance detected by the SSH anomaly. In this mechanism, the disturbance introduces nutrients into the euphotic zone; primary production is therefore enhanced, and eventually chlorophyll concentration increases in the surface water over the nutrient-enriched area. The nutrient enhancement may occur through the compression of near-surface layers, so that deeper layers richer in nutrients extend into the euphotic zone[16]. Alternatively, it may occur through isopycnal mixing within a tilted constant-density layer that protrudes into the euphotic layer over the disturbance[17]. There may also be a physiological delay between the introduction of the nutrients and the enhancement in chlorophyll concentration. For large-scale disturbances that have periods on the order of months, the phase offset caused by such delays should be very small, and unlikely to change much even as the anomaly propagates through areas of different planktonic community structures. The chlorophyll anomaly induced through this mechanism by a SSH anomaly should be easily detected with our methods.

The coherence between SSH and chlorophyll that we observe is consistent with the eddy pumping mechanism, but does not yet prove it: there are means other than enhanced primary production by which the coherence may be created. One of these is the advection of a horizontal background chlorophyll gradient by the geostrophic velocity associated with the baroclinic anomaly. In this case, chlorophyll acts as a passive tracer and the contrast visible in the imagery will be determined by the magnitude of the gradient and its displacement by the disturbance. Another possible mechanism is the shoaling of a deep chlorophyll maximum by the disturbance from an original depth too deep to be seen by the sensor. In the interior of the gyres, where the horizontal chlorophyll gradients are weak and the deep chlorophyll maximum occurs at greater depths, neither of these alternative mechanisms would be very effective. The presence of propagating chlorophyll anomalies in these areas supports the hypothesis of enhanced primary productivity. □

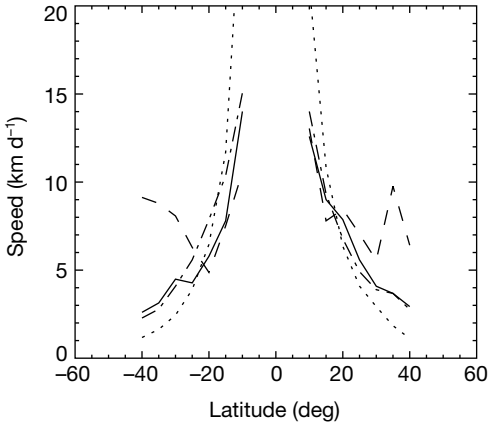

Figure 3 Propagation speeds of Chl and SSH anomalies. The figure shows that propagation speeds of chlorophyll anomalies associated with baroclinic features vary with latitude in nearly the same way as do the theoretical phase speeds of Rossby waves (dotted lines). The propagation speeds are estimated from the wavenumber spectra of chlorophyll (dash-dot line), sea surface height (SSH; dashed line) and chlorophyll–SSH coherence (solid lines) in the Pacific Ocean. The theoretical speeds are based on baroclinic radii of deformation from ref. 15.

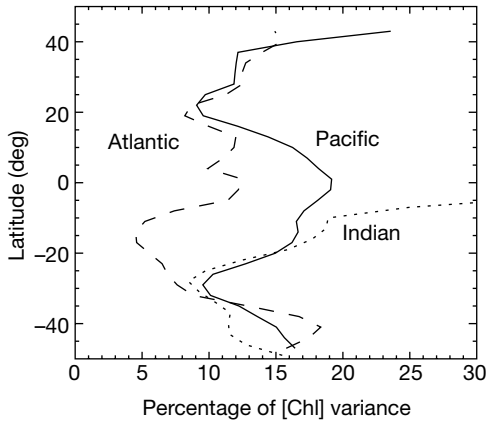

Figure 4 Features associated with westward-propagating baroclinic disturbances make up ~10% of the variance of the log(chlorophyll concentration) data. These chlorophyll data were filtered so as to eliminate variability at length scales larger than 25° and timescales longer than 260 d.

Methods

We acquired individual global area coverage swaths of SeaWiFS chlorophyll concentration from September 1997 to the end of December 1999, and mapped them to a cylindrical grid at 0.125° × 0.125° resolution. We used a median filter over a running box of 21 d and 2° × 2° to filter out small-scale variability and noise. At this stage we also reduced the resolution to 1° × 1° and 10 d. The data were log-transformed and run through Remez highpass filters[18] in longitude (cut-off length scale 25°) and time (cut-off period 260 d) so as to eliminate seasonal and other large-scale variability.

Gridded sea-level anomalies at 0.25° × 0.25° and 10 d resolution calculated by blending TOPEX/POSEIDON and ERS-2 data were supplied by AVISO (Analysis, Validation and Investigation of Satellite Oceanography). This is an optimally analysed data set, which combines some of the strengths of the two platforms, namely better temporal resolution with TOPEX and smaller cross-track separation with ERS-2. The SSH data were highpass-filtered in the same way as chlorophyll.

We calculated the power spectra of, and the coherence between, chlorophyll and SSH records from time–longitude plots individually for each ocean basin at every 5° of latitude between 40° S and 40° N. We averaged the auto-spectra and the co-spectrum over a 3° latitude band, and smoothed over a moving box of three frequencies and three wavenumbers for statistical convergence. (The equivalent number of degrees of freedom was 9.45 after accounting for the reduction in independence of neighbouring spectral bands due to zero padding and cosine-taper windowing.) Coherence was calculated only where both chlorophyll and SSH power spectral densities were at least 1% of their maximum values.

We used the coherence spectra to construct a filter in the frequency–wavenumber domain. The passband of the filter included only the second and fourth quadrants, where the propagation is westward, and only those wavenumbers and frequencies for which the chlorophyll–SSH coherence was above a threshold of 0.3, which was the 95% confidence limit for significant coherence for the number of degrees of freedom in the spectral analysis[19]. This filter was applied to the power spectra of chlorophyll and SSH. The variances of the filtered and unfiltered signals were calculated by integration over wavenumber and frequency.

To estimate the propagation speed of chlorophyll anomalies, we used the 'Radon' transform of the power spectrum or of the SSH–chlorophyll coherence. The Radon transform of a two-dimensional image corresponds to the projection of the image intensity along a radial line oriented at a specified angle[20]. The angle that maximizes the Radon transform is perpendicular to the spectral distribution of the non-dispersive Rossby waves.

The dispersion relation of baroclinic Rossby waves is $\omega = -\beta k(k^2 + \lambda_n^{-2})^{-1}$, where ω is the natural frequency, β is the rate of change of the Coriolis parameter with meridional displacement and λ_n is the radius of deformation for the nth vertical mode. The radius of deformation is a variable of the Coriolis parameter, density stratification and the total depth of the water column. We used λ_n values calculated in ref. 15 using climatological density profiles.

The phase speed ($C_p = \omega / k$) is nondispersive for long waves and equal to $-\beta\lambda_n^2$. We zonally averaged the radii of deformation, which was originally at 1° × 1° resolution within each basin so as to get one mean phase speed at each latitude.

Received 29 March; accepted 6 November 2000.

1. Barber, R. T. in *Primary Productivity and Biogeochemical Cycles in the Sea* (eds Falkowski, P. G. & Woodhead, A. D.) 89–106 (Plenum, New York, 1992).
2. Jenkins, W. J. & Goldman, J. C. Seasonal oxygen cycling and primary production in the Sargasso Sea. *J. Mar. Res.* **43,** 465–491 (1985).
3. McGillicuddy, D. J. Jr & Robinson, A. R. Eddy-induced nutrient supply and new production in the Sargasso Sea. *Deep-Sea Res.* **44,** 1427–1450 (1997).
4. Siegel, D. A., McGillicuddy, D. J. Jr & Fields, E. A. Mesoscale eddies, satellite altimetry and new production in the Sargasso Sea. *J. Geophys. Res.* **104,** 13359–13379 (1999).
5. McGillicuddy, D. J. Jr *et al.* Mesoscale variations of biogeochemical properties in the Sargasso Sea. *J. Geophys. Res.* **104,** 13381–13394 (1999).
6. McGillicuddy, D. J. Jr, Kosnyrev, V. K., Ryan, J. P. & Yoder, J. A. Covariation of mesoscale ocean color and sea surface temperature patterns in the Sargasso Sea. *Deep-Sea Res.* (in the press).
7. Chelton, D. M & Schlax, M. Global observation of oceanic Rossby waves. *Science* **272,** 234–238 (1996).
8. Stammer, D. Global characteristics of ocean variability estimated from regional TOPEX/POSEIDON altimeter measurements. *J. Phys. Oceanogr.* **27,** 1743–1769 (1997).
9. Polito, P. & Cornillon, P. Long baroclinic Rossby waves detected by TOPEX/POSEIDON. *J. Geophys. Res.* **102,** 3215–3235 (1997).
10. Halliwell, G. R. & Cornillon, P. Westward-propagating SST anomaly features in the Sargasso Sea, 1982-88. *J. Phys. Oceanogr.* **21,** 635–649 (1991).
11. Van Woert, M. L. & Price, J. M. Geosat and advanced very high resolution radiometer observations of oceanic planetary waves adjacent to the Hawaiian islands. *J. Geophys. Res.* **98,** 14619–14631 (1993).
12. Cipollini, P. *et al.* Concurrent altimeter and infrared observations of Rossby wave propagation near 34° N in the Northeast Atlantic. *Geophys. Res. Lett.* **24,** 889–892 (1997).
13. McClain, C. R. *et al.* Science quality SeaWiFS data for global biosphere research. *Sea Technol.* **39,** 10–16 (1998).
14. Zang, X. & Wunsch, C. The observed dispersion relationship for North Pacific Rossby wave motions. *J. Phys. Oceangr.* **29,** 2183–2190 (1999).
15. Chelton, D. B. *et al.* Geographical variability of the first baroclinic Rossby radius of deformation. *J. Phys. Oceangr.* **28,** 433–460 (1998).
16. McGillicuddy, D. J. *et al.* Influence of mesoscale eddies on new production in the Sargasso Sea. *Nature* **394,** 263–266 (1998).
17. Hayward, T. L. The nutrient distribution and primary production in the central North Pacific. *Deep-Sea Res.* **34,** 1593–1627 (1987).
18. IEEE *Programs for Digital Signal Processing*, Algorithm 5.1 (IEEE Press, New York, 1979).
19. Emery, W. J. & Thomson, R. E. *Data Analysis Methods in Physical Oceanography* (Pergamon, Oxford/New York, 1997).
20. Lim, J. S. *Two-Dimensional Signal and Image Processing* 42–45 (Prentice Hall, Englewood Cliffs, New Jersey, 1990).

Acknowledgements

We thank the SeaWiFS team for chlorophyll data and AVISO for SSH data; we also thank D. Siegel, P. Polito and S. Schollaert for discussions and recommendations. This work was supported by NASA.

Correspondence and requests for materials should be addressed to B.M.U. (e-mail: m.uz@gso.uri.edu).

Aerogeophysical measurements of collapse-prone hydrothermally altered zones at Mount Rainier volcano

Carol A. Finn*†, Thomas W. Sisson†‡ & Maryla Deszcz-Pan*

* *US Geological Survey, MS964, PO Box 25046, Denver Federal Center, Denver, Colorado 80225, USA*

‡ *US Geological Survey, 345 Middlefield Rd, Menlo Park, California 94025, USA*

† *These authors contributed equally to this work.*

Hydrothermally altered rocks can weaken volcanoes, increasing the potential for catastrophic sector collapses that can lead to destructive debris flows[1]. Evaluating the hazards associated with such alteration is difficult because alteration has been mapped on few active volcanoes[1–4] and the distribution and severity of subsurface alteration is largely unknown on any active volcano. At Mount Rainier volcano (Washington, USA), collapses of hydrothermally altered edifice flanks have generated numerous extensive debris flows[5,6] and future collapses could threaten areas that are now densely populated[7]. Preliminary geological mapping and remote-sensing data indicated that exposed alteration is contained in a dyke-controlled belt trending east–west that passes through the volcano's summit[3–5,8]. But here we present helicopter-borne electromagnetic and magnetic data, combined with detailed geological mapping, to show that appreciable thicknesses of mostly buried hydrothermally altered rock lie mainly in the upper west flank of Mount Rainier. We identify this as the likely source for future large debris flows. But as negligible amounts of highly altered rock lie in the volcano's core, this might impede collapse retrogression and so limit the volumes and inundation areas of future debris flows. Our results demonstrate that high-resolution geophysical and geological observations can yield unprecedented views of the three-dimensional distribution of altered rock.

Mount Rainier (Fig. 1), built in the past ~500 kyr atop Tertiary granitic and metavolcanic rocks[9], is composed of andesite and dacite lavas with subordinate pyroclastic flow deposits[10]. Alteration at the summit lies in the volcano's axial vent system (S, Fig. 1a), through which most magmas that fed the volcano were erupted. Intense alteration (yellow pixels, Fig. 1a) on the volcano's upper flanks is associated with a zone of open fractures and radial dykes[3] (Fig. 1a) emplaced during two episodes of heightened magmatic activity from ~500–400 kyr and ~280–190 kyr[10]. Isotopic evidence suggests that most of the alteration was formed where degassing magmas interacted with meteoric water near the surface (R. Rye, personal communication), supporting the geological and geochronological evidence that alteration on the volcano was confined to